



Graphene grown on stainless steel as a high-performance and ecofriendly anti-corrosion coating for polymer electrolyte membrane fuel cell bipolar plates



Nen-Wen Pu ^{a,1}, Gia-Nan Shi ^{b,c,1}, Yih-Ming Liu ^d, Xueliang Sun ^e, Jeng-Kuei Chang ^f, Chia-Liang Sun ^{g,h,**}, Ming-Der Ger ^{d,*}, Chun-Yu Chen ^b, Po-Chiang Wang ^c, You-Yu Peng ^c, Chia-Hung Wu ^c, Stephen Lawes ^e

^a Department of Photonics Engineering, Yuan Ze University, Zhongli, Taoyuan 320, Taiwan

^b Chemical System Research Division, National Chung Shan Institute of Science and Technology, Longtan, Taoyuan 325, Taiwan

^c School of Defense Science, Chung Cheng Institute of Technology, National Defense University, Dasi, Taoyuan 335, Taiwan

^d Department of Chemical & Materials Engineering, Chung Cheng Institute of Technology, National Defense University, Dasi, Taoyuan 335, Taiwan

^e Department of Mechanical and Materials Engineering, University of Western Ontario, London, ON N6A 5B9, Canada

^f Institute of Materials Science and Engineering, National Central University, 300 Jhongda Road, Taoyuan County, Taiwan

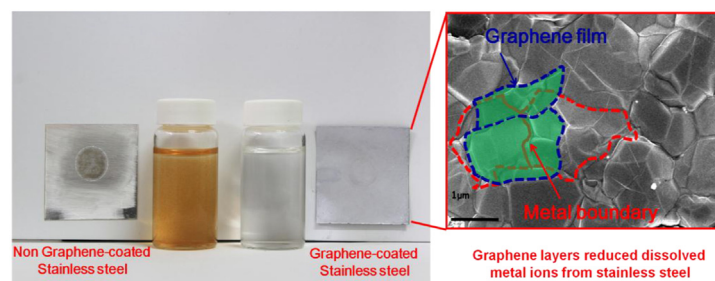
^g Department of Chemical and Materials Engineering, Chang Gung University, Kwei-Shan, Tao-Yuan 333, Taiwan

^h Portable Energy System Group, Green Technology Research Center, Chang Gung University, Kwei-Shan, Tao-Yuan 333, Taiwan

HIGHLIGHTS

- The graphene coating on stainless steel can enhance its anti-corrosion property.
- The pre-plated nickel layer can help graphene completely cover stainless steel surface.
- The graphene coating on stainless steel exhibits a low interfacial contact resistance.

GRAPHICAL ABSTRACT



ARTICLE INFO

Article history:

Received 6 November 2014

Received in revised form

14 January 2015

Accepted 9 February 2015

Available online 11 February 2015

Keywords:

Graphene
Stainless steel
Corrosion

ABSTRACT

In this study, the growth of graphene by chemical vapor deposition (CVD) on SUS304 stainless steel and on a catalyzing Ni/SUS304 double-layered structure was investigated. The results indicated that a thin and multilayered graphene film can be continuously grown across the metal grain boundaries of the Ni/SUS304 stainless steel and significantly enhance its corrosion resistance. A 3.5 wt% saline polarization test demonstrated that the corrosion currents in graphene-covered SUS304 were improved fivefold relative to the corrosion currents in non-graphene-covered SUS304. In addition to enhancing the corrosion resistance of stainless steel, a graphene coating also ameliorates another shortcoming of stainless steel in a corrosive environment: the formation of a passive oxidation layer on the stainless steel surface that decreases conductivity. After a corrosion test, the graphene-covered stainless steel continued to exhibit not only an excellent low interfacial contact resistance (ICR) of 36 mΩ cm² but also outstanding

* Corresponding author. Department of Chemical & Materials Engineering, Chung Cheng Institute of Technology, National Defense University, Dasi, Taoyuan 335, Taiwan.

** Corresponding author. Department of Chemical and Materials Engineering, Chang Gung University, Kwei-Shan, Tao-Yuan 333, Taiwan.

E-mail addresses: sunchialiang@gmail.com (C.-L. Sun), mingderger@gmail.com (M.-D. Ger).

¹ G.N. Shi and N.W. Pu contributed equally to this work.

1. Introduction

At present, most bipolar plates for fuel cells are made of graphite. Graphite is an excellent electrode material because of its low electrical resistance, resistance to corrosion, and physical and chemical stability. However, graphite is brittle and has poor mechanical properties; therefore, it cannot withstand use in mobile products or other applications involving vibrating environments. In addition, it is difficult to mechanically produce gas-flow channels in thin graphite plates, which can break during fuel-cell assembly. Therefore, to achieve the mechanical strength required during fuel-cell assembly, graphite bipolar plates must often be relatively thick; this requirement increases the weight and volume of fuel cells, limiting their applications and causing difficulties in the mass production of fuel cells [1]. Graphite bipolar plates represent more than 80% of the total weight and more than 45% of the total manufacturing costs for proton-exchange-membrane fuel cells [2]. If metals could be used to replace graphite bipolar plates, then the volumes and manufacturing costs of fuel cells could be significantly reduced [3].

Because of its low cost and good corrosion resistance, stainless steel is regarded as one potential material to replace graphite in bipolar plates. However, in the harsh environment of a fuel cell, a passive layer forms on the surface of stainless steel; this passive layer resists corrosion but increases the electrical impedance of the bipolar plates and lowers the power-generation efficiency of the fuel cell [4]. Many researchers have investigated how stainless steel surfaces might be modified with carbon materials to simultaneously satisfy the requirements of high corrosion resistance and low impedance. Some scholars have used chromium carburization to form a chromium–carbon protective layer on the surface of stainless steel [5,6]. However, when chromium powder reacts with carbon atoms to form chromium–carbon compounds, a chromium oxide layer readily forms, increasing contact resistance. The experiments of Wind et al. have demonstrated that gold-coated stainless steel exhibited the same properties as graphite plates in a 1000-h single-cell test; however, the high cost of gold poses a hindrance to the widespread use of gold-coated material [7]. Chung et al. have used an acetylene/hydrogen gas mixture to grow a graphite layer on a nickel/stainless-steel surface; during this process, the carbon atoms initially formed filamentous or spherical carbon structures on the nickel grain boundaries [8]. Fukutsuka et al. has used plasma-enhanced chemical vapor deposition (PECVD) to form a carbon film layer on stainless steel; the carbon material grown disclose distinctly Raman structural defects spectrum [9].

In recent years, graphene has attracted a great deal of research attention because of its outstanding physical properties, such as its high electrical conductivity, high heat-transfer rate, and high specific surface area [10–15]. In the past, graphene nanofilms have primarily been used in transparent conductive films [16] and in transistors [17]. Recent studies have demonstrated that graphene can be used as a protective layer on metal surfaces from gas penetration [18–21], oxidation [22–24], and corrosion [25]. Several approaches, such as CVD, the Langmuir–Blodgett (LB) method, electrodeposition (ED), and electrospray [24,26–30], have been proposed to fabricate two-dimensional graphene coatings on solid

substrates. Compared to CVD, solution-based methods are simple and cost-effective ways to make reduced graphene oxide (rGO) coatings, and have been used for a variety of applications such as the bipolar plates in fuel cells. However, the Raman spectrum of rGO clearly revealed structural defects [28], which would be the active sites for corrosion to occur. In addition, the binder, dispersing agent, or other nonconductive molecules deposited along with rGO usually would increase the contact resistance of the bipolar plates [27,31]. Some researchers have used CVD to grow graphene on nickel and copper substrates [24,32,33]. Various metal catalysts [34–37] and alloys [38–40] have been utilized to catalyze the decomposition of carbon source gases that cause carbon atoms to form single or multiple graphene layers on the metal surface during CVD. Krishnamurthy has used graphene grown on porous nickel foam as electrodes in microbial fuel cells [41]. Some study have also showed that the coverage of copper plates with graphene could effectively reduce short-term air oxidation rates; however, structural defects in the graphene became channels through which oxygen could contact the copper surface, and thus the graphene coating accelerated the long-term oxidation rates of the copper surfaces [42,43]. In 2014, Hsieh et al. used atomic layer deposition (ALD) to deposit aluminum oxide at graphene defects, thereby enhancing the corrosion resistance of graphene/Cu [44]. In the present study, we investigated the reactions of two stainless steel specimens, SUS304 and Ni/SUS304, with methane in a high-temperature environment. With a facile design involving a catalytic metal on stainless steel to control the carbon diffusion process, multiple protective layers of graphene with 100% surface coverage were grown directly on the stainless steel surface and provide excellent anti-corrosion properties and high conductivity.

2. Experimental

2.1. Preparation of the specimen

A nickel layer of 5 μm in thickness was electroplated onto a $4 \times 4 \text{ cm}^2$ SUS304 stainless steel plate with a thickness of 0.5 mm. The specimen was placed in a quartz tube and argon gas (100 sccm) and hydrogen gas (50 sccm) were inlet into this tube. Over 30 min of heating, the temperature was increased from room temperature to a predetermined target temperature (700, 800, or 900 $^{\circ}\text{C}$). When this target temperature was reached, methane gas (25 sccm) was inlet into the quartz tube. After the reaction was complete, only the input of the methane gas was terminated; the flow of the argon/hydrogen gas mixture into the quartz tube was continued until the tube had cooled to room temperature.

2.2. TEM and SEM

The morphology and structure of the as-deposited graphene were characterized with field-emission scanning electron microscopy (FESEM) (LEO 1530) and high-resolution transmission electron microscopy (HRTEM) (Philips Tecnai F30). The SEM micrographs were obtained at 20 kV and a working distance of 15 mm. The TEM was operated at an acceleration voltage of 200 kV.

The TEM samples were prepared using focused ion beam (FIB) (FEI Helios 400) micromachining. The FIB lamellae preparation

method for front view observations is composed of 4 steps: (i) the deposition of the protective material onto the specimen surface in the selected area; (ii) the ion beam rough milling at the front and back sides of the target at an acceleration voltage of 30 kV and a beam current of 2.8 nA; (iii) the TEM lamella was then picked up and fixed on the TEM sample grid by the internal probe; and (iv) the final fine milling (5 kV, 0.11 nA) to ~100 nm in thickness by FIB.

2.3. Raman spectroscopy

Raman spectroscopy was performed with a Renishaw in Via Raman microscope, using a laser excitation wavelength of 514.5 nm, laser power of 12 mW, scan range of 1000–3000 cm^{-1} , 10 s scan time per spot. The size of the focal spot of the laser was 1 μm .

2.4. Electrochemical tests

Polarization testing was carried out with an Autolab PGSTAT30 potentiostat equipped with a frequency response analyzer. Ag/AgCl was used as the reference electrode, and Pt was used as the counter electrode. The standard reduction potential corresponding to the standard hydrogen electrode (SHE) was 0.199 V. The working electrode (WE) was connected to the specimen. Polarization-curve measurements were performed in a 3.5 wt% NaCl solution at ambient temperature. The tested area was 1.76 cm^2 and the scan rate was 5 mVs^{-1} .

2.5. Interfacial contact resistance measurement (ICR)

The setup consisted of a hydraulic press with a load capacity of 25 kN, a load sensor with a measurement range of 0–25 kN and an accuracy of 0.1%, a micro-ohmmeter with a resolution of 0.1 $\mu\Omega$. The experimental setup was used to obtain the constitutive relation between the contact resistance and pressure. The stainless steel was sandwiched between two flat carbon paper of the same material and processing conditions as the bipolar plate. The sandwiched carbon papers/stainless steel assembly were then placed between two copper plates. The range of the operating load was 0–196 N cm^{-2} for recording ICR values at every 9.8 N cm^{-2} .

2.6. X-ray diffraction

X-ray diffraction patterns were obtained with a Bruker D2 Phaser (copper target, characteristic wavelength: 1.54 Å), using a voltage of 30 kV, a current of 20 mA, a scan rate of 1° every 6 s, and a scan range of 20–90°.

2.7. Surface roughness measurement

Surface roughness was measured using a Chroma 7502 white-light interferometer (WLI), with a vertical resolution of 0.1 nm and horizontal resolution of 0.5 μm .

3. Results and discussion

Raman spectra presented in Fig. 1(a) indicate that a few layers of graphene ($I_{2D}/I_G \sim 0.5$) were grown on both SUS304 and Ni/SUS304. In images of the actual specimens (Fig. S1), the surface of the G/SUS304 specimen (Fig. S1(b)) appeared dark gray, whereas the surface of the G/Ni/SUS304 specimen (Fig. S1(c)) appeared silvery gray. Scanning electron microscopy (SEM) was used to examine the differences in the surface morphologies of the two specimens. Although the G/SUS304 specimen without pre-plated Ni exhibited a Raman signal indicative of graphene, Fig. 2(a, b) present little

visual evidence that the metal surface of this specimen was covered by graphene. By contrast, the surface of the G/Ni/SUS304-900-4hr specimen appeared to be completely covered by graphene (Fig. 2(c–e)). In Fig. 2(f), the red dashed lines indicate the boundaries of metal grains on the specimen surface, whereas the blue dashed lines indicate ripples associated with the graphene surface. It suggests that the graphene film grew continuously across the metal grain boundaries. Because of the large differences in the thermal-expansion coefficients of the metal and the graphene, ripples were generated in the surface of the graphene after rapid cooling. For comparison, Gullapalli and John et al. have used hexane and ethanol gas as reaction precursors for the growth of graphene films on stainless steel foil; however, these authors did not discuss the completeness of the graphene coverage or the distribution of the layers of graphene growth [45,46]. We further examined the Ni/SUS304-900-4hr and SUS304-900-4hr specimens in a stepwise fashion by Raman mapping (size of mapping area: 10 $\mu\text{m} \times 10 \mu\text{m}$). Fig. 1(b) and (c) present the G-peak Raman mapping spectra for the G/SUS304-900-4hr and G/Ni/SUS304-900-4hr specimens, respectively. Fig. 1(b) demonstrates that G/SUS304-900-4hr exhibited a weak G-peak signal (signal intensity: <1000), and even in some spots signals were not detected; this finding indicates that there was a low degree of graphenization on the specimen surface. In contrast, Fig. 1(c) reveals that the G/Ni/SUS304-900-4hr specimen exhibited an intense (signal intensity: 3000–8000) and continuous G-peak signal. The electroplated nickel layer of the Ni/SUS304 specimen played a buffering role by reducing the contact of the methane with the various metal elements in the stainless steel directly. From the Raman mapping in Fig. 1(c) and the SEM image in Fig. 2(e), it appears that, unlike the G/SUS304 specimen, the double-layered G/Ni/SUS304 specimen permitted the complete and continuous growth of a graphene layer on the stainless steel surface. Fig. 1(d) demonstrates that the I_{2D}/I_G ratio for graphene was between 0.4 and 1.0, indicating that the stainless steel surface was covered by two or more layers of graphene. Multiple graphene layers and high graphene coverage can yield metals with excellent corrosion resistance [32,47]. Fig. 1(e) provides a high-resolution transmission electron microscopy (TEM) image of the G/Ni/SUS304-900-4hr specimen; the left side of this figure displays the clear orientation of the lattice on the surface of the stainless steel, and shows that the metal surface was covered by multiple graphene layers (marked with red (in the web version) lines). Fig. 1(f) indicates that graphene could still grow on a metal surface that was not completely even, extending along the metal surface to provide a complete coating. The robust growth of the protective graphene coating explains why the underlying stainless steel surface of the Ni/SUS304-900-4hr specimen could be fully protected from corrosion and oxidation.

In addition, we observed an unusual phenomenon (presented in Fig. 1(a)): after the Ni/SUS304 specimen had reacted with methane for 1 h in a 900 °C environment, it was difficult to detect Raman spectroscopy signals indicative of the carbon structure. Nickel is a strongly active metal and has high solubility of carbon that can readily catalyze the pyrolysis of carbon source gases. For these reasons, nickel has been widely used for the growth of graphene via CVD. In a high-temperature environment (900–1000 °C), the growth of single or multiple layers of graphene can occur on the surface of nickel foil after 5–10 min of reaction with methane [35]. However, there are large differences between the reaction mechanisms for the deposition of nickel on stainless steel and the mechanisms for the reaction between methane and nickel metal alone. Wang et al. have proposed that under high-temperature conditions, a deposition reaction occurs between the carbon atoms in carbon steel and chromium powder to form chromium iron carbides, $(\text{Cr, Fe})_x\text{C}_y$ [48,49]. The X-ray diffraction (XRD) results

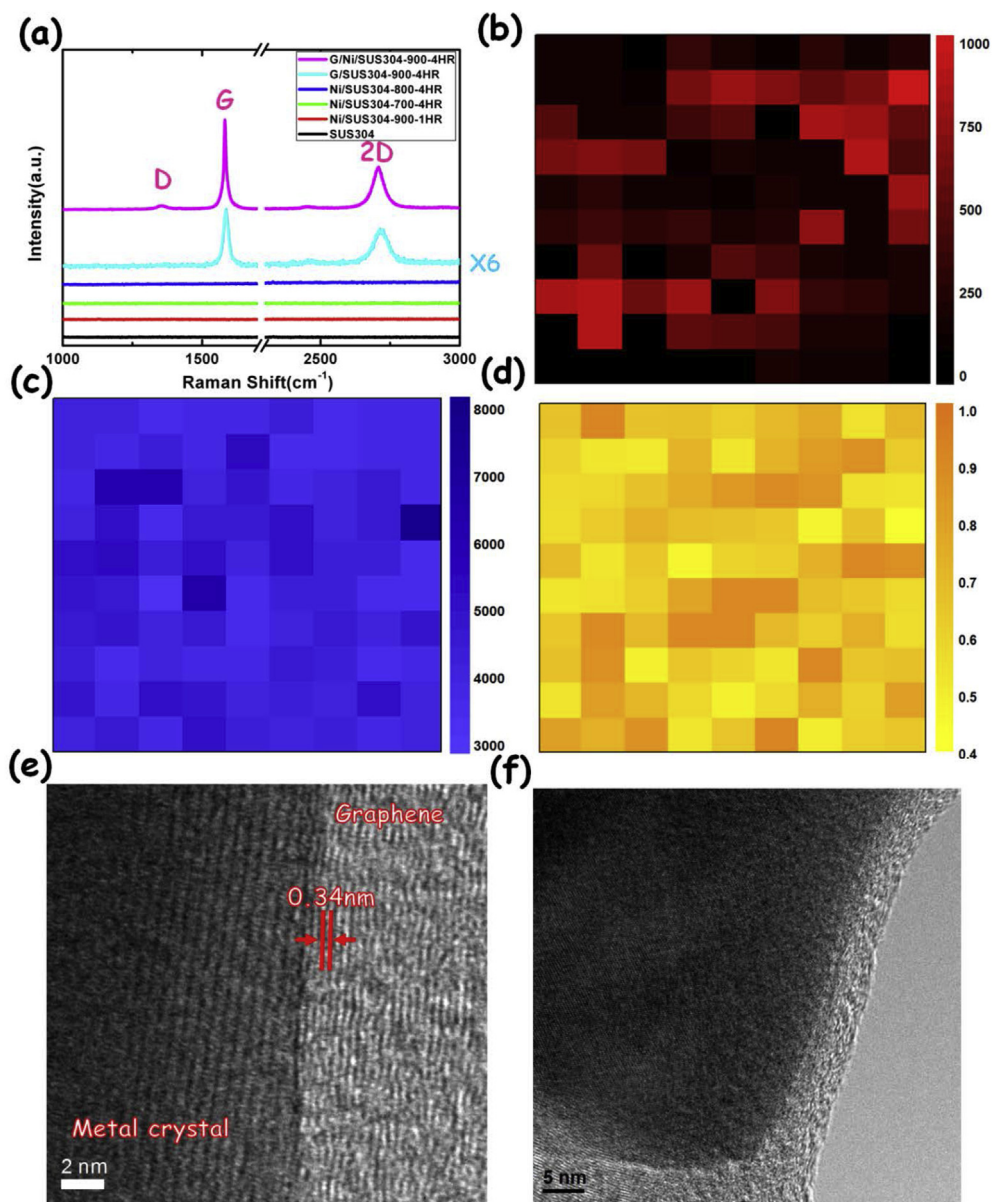


Fig. 1. (a) Raman spectra; (b, c) G Raman peak mapping of G/SUS304-900-4hr and G/Ni/SUS304-900-4hr, respectively; (d) I_{2D}/I_c Raman peak mapping of G/Ni/SUS304-900-4hr; (e, f) cross-sectional TEM image of G/Ni/SUS304-900-4hr.

presented in Fig. S2 demonstrate that after prolonged reaction with methane, a variety of metal carbides, consisting mainly of Cr_3C_2 , Cr_7C_3 , and Fe_2C , had formed on the surfaces of the G/SUS304-900-4hr and Ni/SUS304-900-4hr specimens. Because of the formation of the metal carbide components, after reacting with the methane the surface roughness of the SUS304 and Ni/SUS304 samples increased from 29 nm and 139 nm to 137 nm and 178 nm, respectively (Fig. S3). We concluded that the reactions with the carbon source gas were only weakly catalyzed because SUS304 contains only 8–11% Ni (Table S1); after the pyrolysis of the methane, most of the available carbon atoms preferentially reacted with chromium and iron in the metal to form chromium iron carbides, whereas only an extremely small quantity of carbon atoms precipitated to form graphene. For this reason, the graphene film that was produced after 4 h of reaction between SUS304 and methane gas was insufficient to completely cover the stainless steel surface (Fig. 1(b)). By comparison, the nickel coating of the Ni/

SUS304 increased the rate of reaction between the methane gas and the SUS304. Thus a graphene film that completely covered the stainless steel surface was observed (Figs. 1(c) and 2(e)). In short, the Ni plating fulfilled two functions: (1) it acted as a barrier layer to slow the diffusion of carbon atoms into the stainless steel, lessening the formation of metal carbides and (2) its high catalytic activity and high carbon solubility increased the pyrolysis rate of the carbon source gas, resulting in the formation of multiple graphene layers that completely covered the stainless steel surface (see Fig. 3 for the proposed mechanism).

We used both electrochemical and morphological analysis techniques to investigate the passivation effects on the tested specimens. The potentiodynamic polarization method was used to investigate corrosion phenomena for the SUS304, G/SUS304-900-4hr, and G/Ni/SUS304-900-4hr specimens in an electrolyte solution. The electrolyte selection was guided by the results of previous studies. In one such study, Prasai et al. used a mild electrolyte

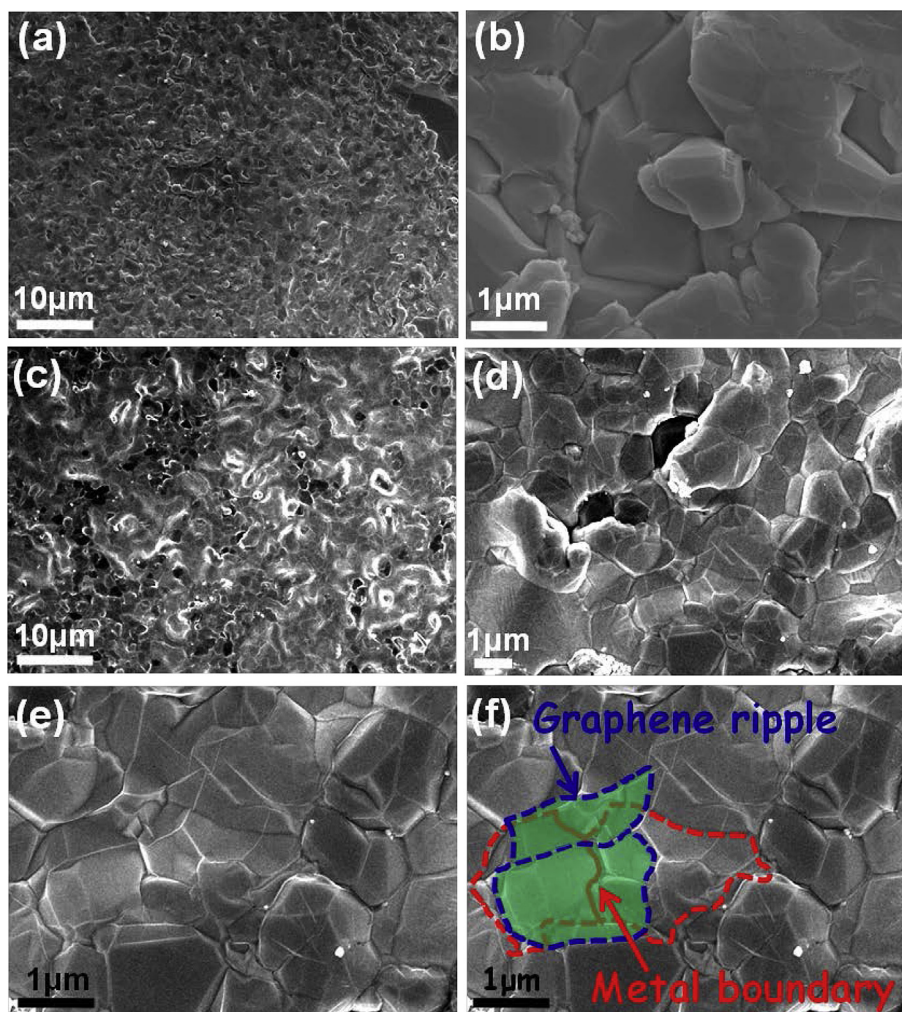


Fig. 2. SEM images (a, b) of G/SUS304-900-4hr; (c, d, e) of G/Ni/SUS304-900-4hr; (f) the red line outlines the metal grain boundary, the blue line outlines the graphene ripples, and the green area shows the metal boundaries covered with a graphene film. (For interpretation of the references to color in this figure legend, the reader is referred to the web version of this article.)

solution (0.1 M NaSO₄) to conduct corrosion resistance tests [32]. Cl⁻, SO₄²⁻, CO₃²⁻, PO₄³⁻, and other anions can severely corrode metals/alloys; in particular, chloride ions exhibit the strongest corrosion capabilities among these anions [47]. In the current study, we used a 3.5 wt. % NaCl solution to test the corrosion resistance of the graphene coating, which possesses a strong corrosive capability and simulates a marine environment. Fig. 4(a) shows the polarization curves of the first scan. The corrosion potentials (E_{corr}) for the SUS304, G/Ni/SUS304-900-4hr, and G/SUS304-900-4hr specimens were 0.04 V, -0.15 V, and -0.32 V, respectively, whereas the corrosion currents (I_{corr}) for these three specimens were 1.49×10^{-7} A-cm⁻², 1.61×10^{-7} A-cm⁻², and 2.32×10^{-6} A-cm⁻², respectively. The corrosion currents remained relatively low for both the SUS304 and G/Ni/SUS304-900-4hr specimens during the first scan. The G/SUS304-900-4hr exhibits the highest corrosion current indicating that its surface has the worst corrosion resistance among all samples. By contrast, because of the lack of complete graphene protection on the surface, the corrosion current of the G/SUS304-900-4hr differed from the corrosion currents of the other two specimens by an order of magnitude. It demonstrates that this specimen was most vulnerable to corrosion. To simulate the long-term of corrosion under laboratory circumstances, the samples were immersed in the

corrosive electrolyte for twenty scans. As Fig. 4(b) indicated, the corrosion current for the SUS304 specimen increased from 10^{-7} to 10^{-6} A-cm⁻², and the corrosion potential decreased from 0.04 V to -0.24 V after twenty polarization scans. When the voltage was raised between -0.13 V and -0.1 V, a passive film formed on the surface of the stainless steel to prevent the continued dissolution of the inner metal. During upward scanning, pits start growing at the pitting potential (0.38 V) in the transpassive region of the polarization curve, where the current increases sharply from the passive current level due to a breakdown of the passive film. As Fig. S4(a) shows, micropores and rust were clearly observed on the testing area of the SUS304 after prolonged corrosion. However, after twenty polarization-curve scans, the corrosion current for the G/Ni/SUS304-900-4hr specimen remained at relatively low corrosion current (10^{-7} A-cm⁻²). No passivation or pitting polarization curve similar to the curve of the SUS304 specimen was observed on the G/Ni/SUS304-900-4hr specimen. The complete surface coverage of the graphene coating, as demonstrated in Fig. 2(e), effectively prevented the chloride-ion-induced corrosion and slowed the occurrence of passivation.

The optical microscopic images presented in Fig. 5 indicate that the surface of the SUS304 was initially bright (Fig. 5(a)), with a lined texture attributable to mechanical processing. After 20 polarization

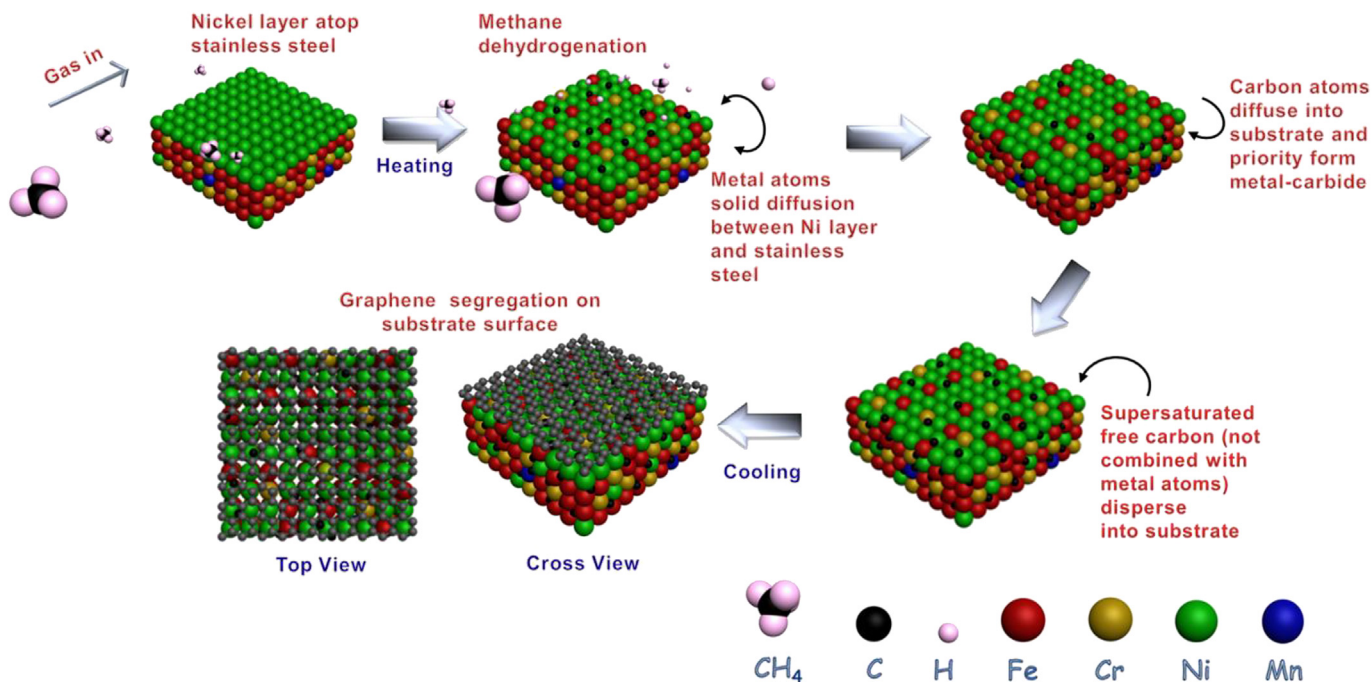


Fig. 3. Schematic diagram of the graphene formation mechanism on Ni/SUS304 substrate.

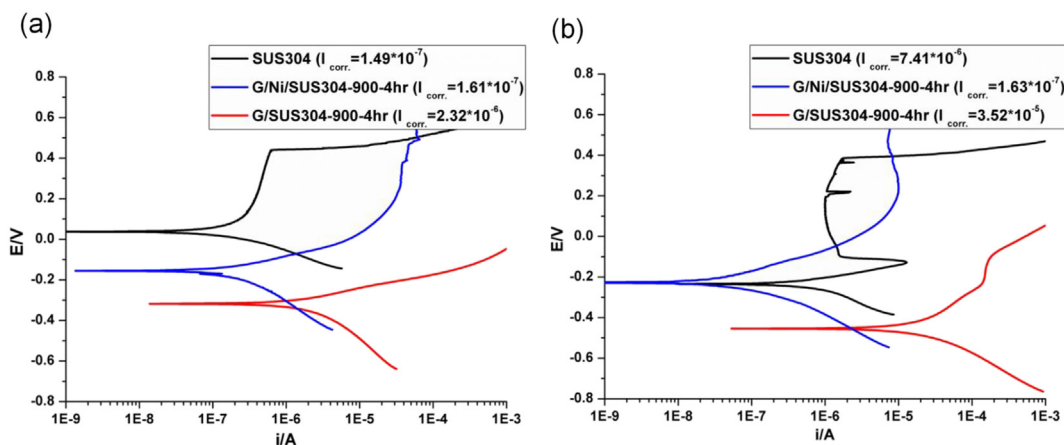


Fig. 4. Tafel plots of SUS304 (black line), G/SUS304-900-4hr (red line), G/Ni/SUS304-900-4hr (blue line) for the (a) first scan and (b) twentieth scan. (For interpretation of the references to color in this figure legend, the reader is referred to the web version of this article.)

tests (Fig. 5(b)), large areas of dark brown rust were present on the sample surface (blue (in the web version) arrows); these corroded, rusty regions covered approximately 60% of the tested surface. Several severely corroded regions and numerous sunken holes with diameters of approximately 10–20 μm were also observed (red (in the web version) arrows). In contrast, Fig. 5(c) reveals that after the G/Ni/SUS304-900-4hr specimen reacted with methane gas in a high-temperature environment, metal carbides were formed on the surface of the specimen, and the roughness of the surface increased. This finding was consistent with the roughness measurement displayed in Fig. S3(d). The optical microscope images show that the dark brown rusty regions and corrosion holes evident on SUS304 (Fig. 5(b)) were not observed on the surface of G/Ni/SUS304-900-4hr after polarization testing (Fig. 5(d)); even an enlarged view of Fig. 5(d) reveals the presence of only a few small, reddish, copper-colored spots of rust on the surface of this

specimen (green (in the web version) arrows). Graphene grown via CVD possesses a polycrystalline structure that is naturally deposited at grain boundaries and folds [42,50,51]. Thus, the observed results may suggest that the passage of chloride ions through structural defects in the graphene occurred after prolonged electrochemical testing.

Another challenge related to the use of metal bipolar plates in fuel cells is that metals become corroded and oxidized after prolonged exposure to a corrosive environment and the resulting dissolved metal ions tend to poison platinum catalysts, reducing their catalytic capabilities. Fe, Cr, and Ni ions, among other metal ions, will poison such catalysts; in particular, an increase in the iron-ion concentration not only affects the catalytic activities of catalysts but may also cause a dramatic decrease in the conductivity of proton-exchange membranes [52–55]. Fig. S4(b) and (c) indicate that after 20 polarization tests, the electrolyte solution for the

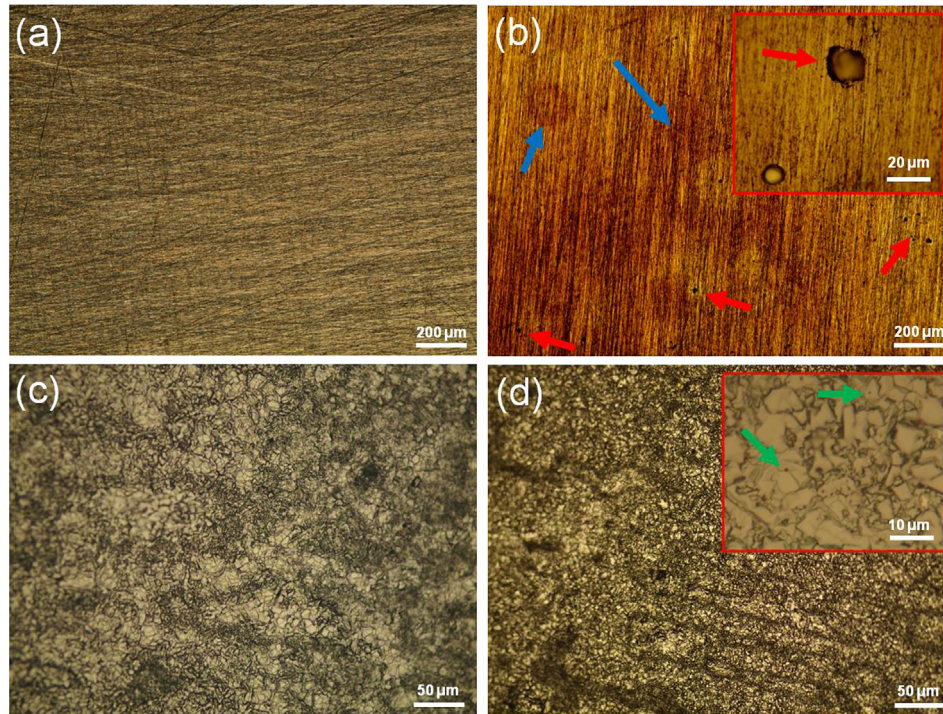


Fig. 5. Optical microscopy images of (a) SUS304, (b) SUS304 after polarization (inset: a local enlarged view), (c) G/Ni/SUS304-900-4hr, (d) G/Ni/SUS304-900-4hr after polarization (inset: a local enlarged view).

graphene-protected G/Ni/SUS304-900-4hr stainless steel specimen remained clear; by contrast, because of the release of various metal ions as a result of the oxidation of the specimen structure, the electrolyte solution for the non-graphene-protected SUS304 stainless steel specimen had changed from transparent to a yellowish-brown color. Inductively coupled plasma (ICP) was used to analyze the types and concentrations of metal ions in the electrolyte solutions. In the SUS304 electrolyte solution, iron, chromium, and nickel metal ions were detected at concentrations of 29 ppm, 6 ppm, and 2 ppm, respectively; however, in the G/Ni/SUS304-900-4hr electrolyte solution, no Fe, Cr, or Ni ions could be detected using an instrument with a lower limit of detection of 0.1 ppm. Therefore, it was evident that the protective graphene layer effectively reduced the concentration of dissolved metal ions released from the stainless steel and thereby slowed the rate of proton-exchange-membrane poisoning.

In addition to corrosion resistance, the low impedance of metal bipolar plates could help to reduce losses in the overall output power of fuel cells. We observed changes in the contact resistances of the SUS304 and G/Ni/SUS304-900-4hr specimens before and after polarization testing. Fig. 6(a) indicates that the contact resistance gradually decreased as the compaction force increased. This phenomenon occurred because the number of contact points between the stainless steel coating and the carbon paper increased with increasing compaction force. After corrosion by chloride ions, the contact resistance of the SUS304 specimen increased from $158 \text{ m}\Omega \text{ cm}^2$ to $560 \text{ m}\Omega \text{ cm}^2$ (under a compaction force of 140 N cm^{-2}), which corresponds to a 250% increase. As depicted in the anodic polarization curve for SUS304 stainless steel shown in Fig. 4, an increase in voltage produced only a small change in current. However, although the metal oxide film that forms on the surface of stainless steel through passivation can slow the corrosion rate, this film also increases the contact resistance, leading to an increase in the internal resistance of the fuel cell and negatively impacting the cell's power-generation efficiency. The graphene

barrier on the surface of the G/Ni/SUS304-900-4hr specimen also slowed the rate of oxidative corrosion; thus, no significant passivation was observed in the anodic polarization curve of this specimen. The experiments revealed that the contact resistance of the Ni/SUS304-900-4hr specimen only slightly increased after polarization testing (Fig. 6(b)); this resistance increased by only 20% (from $30 \text{ m}\Omega \text{ cm}^2$ to $36 \text{ m}\Omega \text{ cm}^2$). A graphene coating with complete surface coverage on stainless steel not only provides corrosion protection but also exhibits excellent electrical conductivity.

During fuel-cell operation, hydrogen ions pass through the proton-exchange membrane to react with oxygen at the cathode to form water. Prolonged fuel-cell use will generate acid anions, such as SO_3^- , SO_4^- , HSO_4^- , and F^- , in the polymer electrolyte membrane. If the contact angle between the material of the bipolar plate and the water is small, the generated water can readily accumulate in the channels of the bipolar plate; this phenomenon may lead to the blocking of these channels and can create an acidic environment that accelerates the corrosion of the bipolar plate, degrading fuel-cell performance. Proper drainage can also help to accelerate the dissipation of heat produced when a fuel cell generates power. Therefore, with respect to fuel-cell performance, the hydrophobicity of the bipolar plates is a critical issue that must be addressed. Because of its non-polar covalent-bond structure, graphene exhibits hydrophobic characteristics that prevent it from engaging in hydrogen bonding with water molecules [56]. As indicated in Fig. 6(c) and (d), contact angle measurements revealed that the presence of a graphene coating increased the angle at which water contacted the stainless steel from 65° to 101° , significantly increasing the hydrophobicity of the stainless steel.

4. Conclusion

In summary, we demonstrate that an optimal CVD process can be used to synthesize a continuous and high-quality graphene thin film on nickel-buffered stainless steel. The nickel barrier on steel is

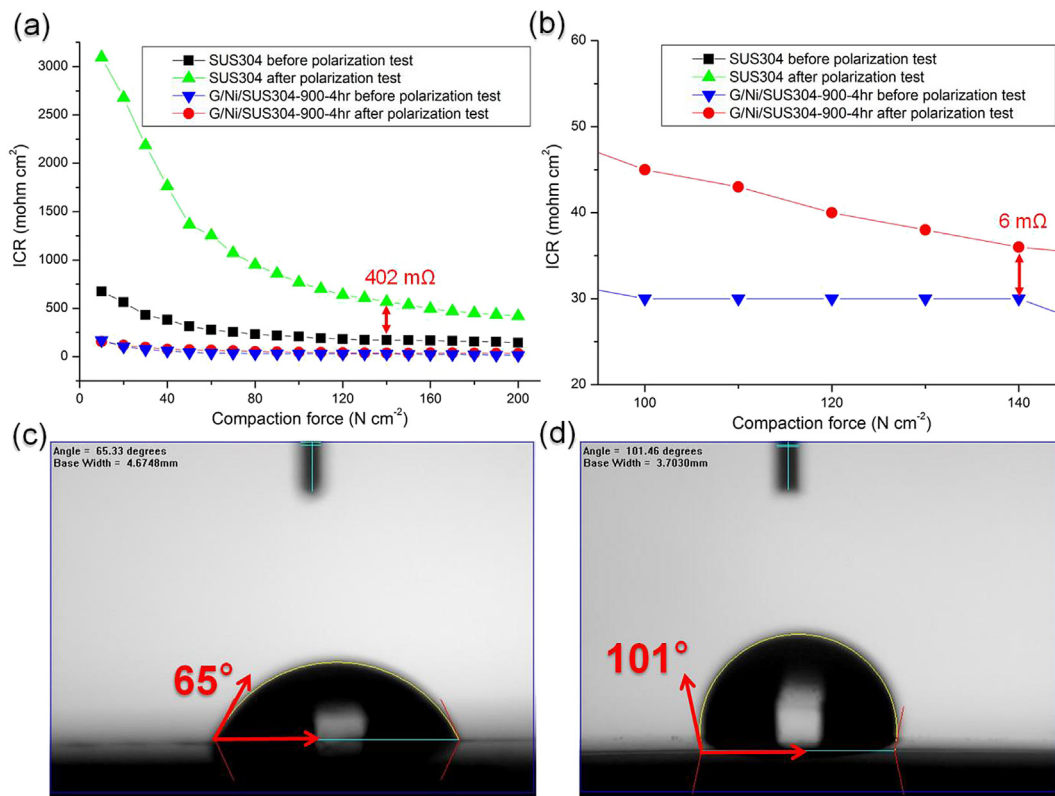


Fig. 6. (a) Plot of interfacial contact resistance against compaction force; (b) an enlarged view of the contact resistance plot (focused on a compaction force of 140 N cm^{-2}); (c, d) water contact angle on SUS304 and G/Ni/SUS304-900-4hr specimens, respectively.

able to both reduce the formation of metal carbide and catalyze graphene precipitation at high temperatures. Thus it successfully solves the poor graphitization issue on bare SUS304 with no buffer layer. Compared with steels without protection, the graphene-coated steel exhibits outstanding anti-corrosion properties, indicating that the multilayered graphene can effectively prohibit the access of chloride ions into the steel surfaces. The graphene coating on steel also maintains good conductivity and increases its hydrophobicity. It is believed that these environmentally friendly graphene-based steel coatings have the potential to replace chrome and other potentially toxic chemicals. In addition, this graphene-coated corrosion-resistant stainless steel could be further utilized in next-generation fuel-cell bipolar plates.

Acknowledgments

This study is sponsored by National Science Council Taiwan under Grant No. NSC102-2917-I-606-001, No. NSC 102-2221-E-606-014, and NSC102-2221-E-155-021. C.S. gratefully acknowledges the financial support from the Chang Gung Memorial Hospital (CMRPD2C0013).

Appendix A. Supplementary data

Supplementary data related to this article can be found at <http://dx.doi.org/10.1016/j.jpowsour.2015.02.055>.

References

- [1] R.C. Makkusub, A.H.H. Janssenb, F.A.D. Bruijnbn, R.K.A.M. Mallant, *Fuel Cells Bull.* 3 (2000) 5–9.
- [2] H. Tsuchiya, O. Kobayashi, *Int. J. Hydrog. Energy* 29 (2004) 985–990.
- [3] H. Tawfik, Y. Hung, D. Mahajan, *J. Power Sources* 163 (2007) 755–767.
- [4] A. Hermann, T. Chaudhuri, P. Spagnol, *Int. J. Hydrog. Energy* 30 (2005) 1297–1302.
- [5] V.V. Nikam, R.G. Reddy, S.R. Collins, P.C. Williams, G.H. Schiroky, G.W. Henrich, *Electrochim. Acta* 53 (2008) 2743–2750.
- [6] S.B. Lee, K.H. Cho, W.G. Lee, H. Jang, *J. Power Sources* 187 (2009) 318–323.
- [7] J. Wind, R. Spah, W. Kaiser, G. Bohm, *J. Power Sources* 105 (2002) 256–260.
- [8] C.Y. Chung, S.K. Chen, P.J. Chiu, M.H. Chang, T.T. Hung, T.H. Ko, *J. Power Sources* 176 (2008) 276–281.
- [9] T. Fukutsuka, T. Yamaguchi, S.I. Miyano, Y. Matsuo, Y. Sugie, Z. Ogumi, *J. Power Sources* 174 (2007) 199–205.
- [10] K.S. Novoselov, A.K. Geim, S.V. Morozov, D. Jiang, M.I. Katsnelson, I.V. Grigorieva, S.V. Dubonos, A.A. Firsov, *Nature* 438 (2005) 197–200.
- [11] K.S. Novoselov, Z. Jiang, Y. Zhang, S.V. Morozov, H.L. Stormer, U. Zeitler, J.C. Maan, G.S. Boebinger, P. Kim, A.K. Geim, *Science* 315 (2007) 1379.
- [12] A.K. Geim, K.S. Novoselov, *Nat. Mater.* 6 (2007) 183–191.
- [13] K.S. Novoselov, V.I. Fal'ko, L. Colombo, P.R. Gellert, M.G. Schwab, K. Kim, *Nature* 490 (2012) 192–200.
- [14] J.N. Shi, M.D. Ger, Y.M. Liu, Y.C. Fan, N.T. Wen, C.K. Lin, N.W. Pu, *Carbon* 51 (2013) 365–372.
- [15] H. Tian, C. Li, M.A. Mohammad, Y.L. Cui, W.T. Mi, Y. Yang, D. Xie, T.L. Ren, *ACS Nano* 8 (2014) 5883–5890.
- [16] S. Bae, H. Kim, Y. Lee, X. Xu, J.S. Park, Y. Zheng, J. Balakrishnan, T. Lei, H.R. Kim, Y.I. Song, Y.J. Kim, K.S. Kim, B. Ozyilmaz, J.H. Ahn, B.H. Hong, S. Iijima, *Nat. Nanotechnol.* 5 (2010) 574–578.
- [17] Y.M. Lin, K.A. Jenkins, A. Valdes-Garcia, J.P. Small, D.B. Farmer, P. Avouris, *Nano Lett.* 9 (2009) 422–426.
- [18] J.S. Bunch, S.S. Verbridge, J.S. Alden, A.M. van der Zande, J.M. Parpia, H.G. Craighead, P.L. McEuen, *Nano Lett.* 8 (2008) 2458–2462.
- [19] R.R. Nair, H.A. Wu, P.N. Jayaram, I.V. Grigorieva, A.K. Geim, *Science* 335 (2012) 442–444.
- [20] O. Leenaerts, B. Partoens, F.M. Peeters, *Appl. Phys. Lett.* 93 (2008).
- [21] H. Kim, Y. Miura, C.W. Macosko, *Chem. Mater.* 22 (2010) 3441–3450.
- [22] L. Liu, S. Ryu, M.R. Tomasik, E. Stolyarova, N. Jung, M.S. Hybertsen, M.L. Steigerwald, L.E. Brus, G.W. Flynn, *Nano Lett.* 8 (2008) 1965–1970.
- [23] S.P. Surwade, Z. Li, H. Liu, *J. Phys. Chem. C* 116 (2012) 20600–20606.
- [24] S. Chen, L. Brown, M. Levendorf, W. Cai, S.Y. Ju, J. Edgeworth, X. Li, C.W. Magnuson, A. Velamakanni, R.D. Piner, J. Kang, J. Park, R.S. Ruoff, *ACS Nano* 5 (2011) 1321–1327.
- [25] H. Xue, T. Wand, Hu Guo, X. Fan, Z. Zhu, X. Pana, J. He, *RSC Adv.* 4 (2014) 57724–57732.
- [26] L.K.P.G. Zhu, T. Lu, T. Xu, Z. Sun, *J. Mater. Chem.* 21 (2011) 14869–14875.

- [27] A.K.S. Subash Chandra Sahu, Madhabi Seth, Shaikh Parwaiz, Bimal P. Singh, Purna C. Rath, Bikash Kumar Jena, *Electrochem. Commun.* 32 (2013) 22–26.
- [28] J.M.P. Ji Hoon Park, *Surf. Coatings Technol.* 254 (2014) 167–174.
- [29] J. Kim, Y.D. Kim, D.G. Nam, *J. Nanosci. Nanotechnol.* 13 (2013) 3387–3391.
- [30] Y.G.A.Y.Y. Brendan Gan, *Adv. Mater. Res.* 905 (2014) 167–170.
- [31] W.L. Wang, S.M. He, C.H. Lan, *Electrochim. Acta* 62 (2012) 30–35.
- [32] D. Prasai, J.C. Tuberquia, R.R. Harl, G.K. Jennings, K.I. Bolotin, *ACS Nano* 6 (2012) 1102–1108.
- [33] N.T. Kirkland, T. Schiller, N. Medhekar, N. Birbilis, *Corros. Sci.* 56 (2012) 1–4.
- [34] P.W. Sutter, J.I. Flege, E.A. Sutter, *Nat. Mater.* 7 (2008) 406–411.
- [35] A. Reina, X. Jia, J. Ho, D. Nezich, H. Son, V. Bulovic, M.S. Dresselhaus, *J. Kong, Nano Lett.* 9 (2009) 30–35.
- [36] X. Li, W. Cai, J. An, S. Kim, J. Nah, D. Yang, R. Piner, A. Velamakanni, I. Jung, E. Tutuc, S.K. Banerjee, L. Colombo, R.S. Ruoff, *Science* 324 (2009) 1312–1314.
- [37] R.M. Jacobberger, M.S. Arnold, *Chem. Mater.* 25 (2013) 871–877.
- [38] B. Dai, L. Fu, Z. Zou, M. Wang, H. Xu, S. Wang, Z. Liu, *Nat. Commun.* 2 (2011).
- [39] R.S. Weatherup, B.C. Bayer, R. Blume, C. Ducati, C. Baetz, R. Schloegl, S. Hofmann, *Nano Lett.* 11 (2011) 4154–4160.
- [40] M.H. Ruemmel, M. Zeng, S. Melkhanova, S. Gorantla, A. Bachmatiuk, L. Fu, C. Yan, S. Oswald, R.G. Mendes, D. Makarov, O. Schmidt, J. Eckert, *Chem. Mater.* 25 (2013) 3880–3887.
- [41] A. Krishnamurthy, V. Gadhamshetty, R. Mukherjee, Z. Chen, W. Ren, H.M. Cheng, N. Koratkar, *Carbon* 56 (2013) 45–49.
- [42] M. Schriver, W. Regan, W.J. Gannett, A.M. Zaniwski, M.F. Crommie, A. Zettl, *ACS Nano* 7 (2013) 5763–5768.
- [43] F. Zhou, Z. Li, G.J. Shenoy, L. Li, H. Liu, *ACS Nano* 7 (2013) 6939–6947.
- [44] Y.-P. Hsieh, M. Hofmann, K.-W. Chang, J.G. Jhu, Y.-Y. Li, K.Y. Chen, C.C. Yang, W.-S. Chang, L.-C. Chen, *ACS Nano* 8 (2014) 443–448.
- [45] H. Gullapalli, A.L.M. Reddy, S. Kilpatrick, M. Dubey, P.M. Ajayan, *Small* 7 (2011) 1697–1700.
- [46] R. John, A. Ashokreddy, C. Vijayan, T. Pradeep, *Nanotechnology* 22 (2011).
- [47] R.K.S. Raman, P.C. Banerjee, D.E. Lobo, H. Gullapalli, M. Sumandasa, A. Kumar, L. Choudhary, R. Tkacz, P.M. Ajayan, M. Majumder, *Carbon* 50 (2012) 4040–4045.
- [48] Z.B. Wang, J. Lu, K. Lu, *Acta Mater.* 53 (2005) 2081–2089.
- [49] L. Yang, H. Yu, L. Jiang, L. Zhu, X. Jian, Z. Wang, *J. Power Sources* 195 (2010) 2810–2814.
- [50] S.J. Chae, F. Guenes, K.K. Kim, E.S. Kim, G.H. Han, S.M. Kim, H.-J. Shin, S.-M. Yoon, J.-Y. Choi, M.H. Park, C.W. Yang, D. Pribat, Y.H. Lee, *Adv. Mater.* 21 (2009), 2328–+.
- [51] K. Kim, Z. Lee, W. Regan, C. Kisielowski, M.F. Crommie, A. Zettl, *ACS Nano* 5 (2011) 2142–2146.
- [52] E.A. Cho, U.S. Jeon, S.A. Hong, I.H. Oh, S.G. Kang, *J. Power Sources* 142 (2005) 177–183.
- [53] M.J. Kelly, B. Egger, G. Faflek, J.O. Besenhard, H. Kronberger, G.E. Nauer, *Solid State Ionics* 176 (2005) 2111–2114.
- [54] M.J. Kelly, G. Faflek, J.O. Besenhard, H. Kronberger, G.E. Nauer, *J. Power Sources* 145 (2005) 249–252.
- [55] A.B. LaConti, M. Hamdan, R.C. McDonald, (2003) 648.
- [56] O. Leenaerts, B. Partoens, F.M. Peeters, *Phys. Rev. B* 79 (2009).